Journal of Energy Storage 109 (2025) 115203

Contents lists available at ScienceDirect

Journal of Energy Storage

journal homepage: www.elsevier.com/locate/est

Research papers

Experimental study on thermal energy storage for thermal power flexibility retrofit combined with waste resource utilization in steel industry: Using single-piece stacking bed as an example

Xiang Liu, Lijia Wei, Laiquan Lv, Hao Zhou *

Zhejiang University, Institute for Thermal Power Engineering, State Key Laboratory of Clean Energy Utilization, Hangzhou 310027, PR China

ARTICLE INFO

Keywords:
TES
Flexible retrofit
Solid particle
Waste utilization
Steam generator

ABSTRACT

A novel method utilizing return fine particles instead of molten salt to enhance the flexibility of thermal power plants has been proposed, which can be connected in series to scale up quickly (like battery). A pilot-scale experimental setup and charging/discharging experiments were constructed to explore the possibilities of combining thermal energy storage (TES) with waste resource utilization in the steel industry. Key findings are as follows: Steam at 250 °C achieved the highest charging power of approximately 10 kW due to its lower particle-specific heat capacity and superior charging capability against ambient temperature, followed by steam at 400 °C, 350 °C, and 300 °C. The highest $\overline{P_c}$ and $\overline{K}$ at 250 °C were 7.42 kW and 314.37 W/(m^2·K), respectively. Steam at 400 °C followed with 5.67 kW and 222.91 W/(m^2·K). Despite its lower specific heat capacity, 250 °C steam had the lowest charging efficiency. Considering multiple indicators, charging at 400 °C showed significant advantages. 350 °C and 400 °C bed continuously produced superheated steam above 250 °C for 12 min, maintaining a power generation of 30 kW. 350 °C bed exhibited the highest discharge efficiency at approximately 75 % due to a more extensive phase transition region and higher steam generation rate. Movement speed and area proportion of the phase transition region at different bed temperatures were determined, with speeds ranging from 10 to 30 mm/s. The phase transition region at 400 °C eventually occupied 75 % of the device volume. Extracting steam above 350 °C for energy storage demonstrated higher charging and discharging efficiency and was suitable for multiple charging cycles, making it the optimal choice in the flexible retrofitting of thermal power plants.

1. Introduction

Global Energy Interconnection Development and Cooperation Organization (GEIDCO) predicts that installed wind and solar power capacity in China will exceed 1200 GW by 2030. The share of clean energy in power generation is projected to increase further by 2060, with the total installed capacity expected to exceed 10,000 GW, which indicates a strong commitment to advancing clean energy development and achieving carbon neutrality in China [1]. Meanwhile, high wind and solar power curtailment rates have led to significant resource waste. Integration of clean energy has become the most prominent challenge in energy development [2]. The volatility and integration issues of renewable energy have increased the market demand for peaking power sources. Thermal power units have become the primary choice for peaking power sources due to their excellent stability. However, the current flexibility of coal-fired power plants does not meet the needs of renewable energy development [3]. In recent years, thermal power plants have proposed enhancing flexibility through energy storage technologies [4]. The main energy storage technologies currently applied in power systems include battery storage, pumped storage, thermal energy storage (TES), and compressed air energy storage. Considering technological maturity and cost-effectiveness, TES has become the preferred choice for thermal power plants [5].

TES reduces unit load by extracting high-temperature steam and storing heat by exchanging heat between superheated steam, flue gas, and the thermal storage medium. During the heat release phase, the stored heat is used to heat feedwater or steam, thereby enhancing the power generation capacity of the unit [6]. Wojcik et al. [7] proposed a flexible operation scheme for a 375 MW oil-fired power plant integrated with TES and presented various heat storage and release schemes at different steam extraction and injection points. The advantages and

---

* Corresponding author.
E-mail address: zhouhao@zju.edu.cn (H. Zhou).

https://doi.org/10.1016/j.est.2024.115203
Received 7 October 2024; Received in revised form 9 December 2024; Accepted 24 December 2024

Nomenclature

Parameters

P	Power, W
Pr	Pressure, Pa
H	Specific enthalpy, kJ/kg
T	Temperature, °C
m	Flow rate, kg/s
K	Total heat transfer coefficient W(m^2·K)
A	Heat transfer area, m^2
R	Thermal resistance, (m^2·K)/W
D	Diameter of the tube, m
λ	Thermal conductivity, W/(m·K)
l	Characteristic length, m
h	Convective heat transfer coefficient W(m^2·K)
η	Efficiency
E	Steam charge/discharge energy J
Cp	Specific heat capacity J/(kg·K)
Ap	Area proportion
Q	Energy absorption/release by solid particles, J
M	Total weight of particles, kg
N	Number of phase transition regions
X	X coordinate of the phase transition area point, m
Y	Y coordinate of the phase transition area point, m
$\bar{q}$	Total heat exchange of the device, J

Subscript

c	Charge
d	Discharge
g	Vapor
in	Inlet
out	Outlet
HTF	Heat transfer fluid
wall	Tube wall
fin	Fin
S	Solid particle
inner	Inner wall of the tube
outer	Outer wall of the tube
conv	Convective
r	Real-time
t	This moment
t'	Charge duration
t''	Discharge duration
1	Charging begins
2	Charging ends
3	End of discharge
l	Subcooled phase
l-g	Vapor-liquid phase

disadvantages of each flexible operation scheme were carefully analyzed, and the results indicated that the integration of TES with the power plant cycle is feasible. Li et al. [8] studied a 420 MW combined gas-vapor cycle, integrating a TES to analyze the dynamic characteristics of the coupled system. Their research demonstrated that the heat storage and release processes significantly enhance the output power and operational flexibility. Liu et al. [9] proposed a model of TES coupled to a coal-fired power plant with a mixed heat source, with a maximum round-trip efficiency of 62.97 %. Miao et al. [10] proposed three models of TES coupled to different locations in a power plant, with a maximum round-trip efficiency of 50.81 %. Zhang et al. [11] proposed a model for improving the flexibility of the cogeneration plant system by using steam ejectors and TES, with an increase in energy efficiency of up to 20.7 %. Li et al. [12] proposed a flexible operation strategy for a supercritical coal-fired power plant integrated with high-temperature TES. Based on SimuEngine simulation software, they introduced three heat storage and two heat release schemes, which involve storing high-temperature steam heat and releasing it into the system by heating feedwater. This simulation model was also applied to the UK grid, and the results indicated that the integrated TES plant has a faster response time to load changes. Tang et al. [13] proposed a system coupling molten salt heat storage with combined heat and power (CHP). The research results showed that integrating TES can increase the maximum and minimum adjustable power loads by 17.13 MW and 12.01 MW, respectively. Liu et al. [14,15] determined the optimal mass flow rates of main steam and reheated steam using MHFlow software and calculated the round-trip efficiency under different operating conditions, which utilizing main steam to inject reheated steam achieved a cycle efficiency of over 80 %. Additionally, Stevanovic et al. [16] proposed an integrated system coupling a steam accumulator with a thermal power plant. A steam accumulator with a volume of 600 m^3 is charged with superheated steam extracted from the high-pressure turbine outlet (at 4.5 MPa pressure and 335 °C temperature). The steam released from the accumulator replaces the turbine steam extraction for two low-pressure heaters, resulting in a power increase of 27.3 MW within 27 min. Richter M. et al. [17] proposed coupling a steam accumulator with a thermal power plant and investigated the dynamic characteristics of the unit during heat storage and release processes using Dymola software. The results showed that using a steam accumulator for energy storage would reduce net power by 7.0 % while releasing energy from the steam accumulator could quickly generate an additional 4.3 % net power.

TES materials can be categorized into three main groups: latent heat, sensible heat, and thermochemical energy storage materials. Sensible TES systems are one of the most promising options in terms of capacity, storage time, and cost, but have a relatively low energy storage density [18]. Phase change materials (PCMs) used in latent heat energy storage systems are promising in terms of energy density and capacity, but are relatively costly [19]. Thermochemical energy storage systems offer the highest energy density but are still at a disadvantage in terms of cost and scale [20]. Cost has become a decisive factor for project executives to consider as the world economy is on a downward spiral. Therefore, more researchers are focusing on solid materials due to the high cost, corrosive, and leaky nature of molten salt [21]. Sensible heat storage using solid materials is gaining popularity due to its reliable stability and economic advantages. This technology has wide applications in various fields, including solar heat storage [22], mobile heating [23], domestic heating [24], cooking [25] and district heating [26]. Among sensible heat storage materials of solid, concrete has a low cost per heat storage unit and is suitable for high-temperature applications. Consequently, existing literature has examined the energy efficiency, cyclic heat storage, and release performance, and influencing factors of concrete heat storage systems [27,28]. High-temperature thermal storage systems exchange heat with the working fluid mainly through embedded channels. [29,30]. Guan et al. [31] studied a steam generator using graphite as the heat storage material, which is charged via electric heating and then releases heat to generate steam for heating or enhance power plant flexibility. Building on this, Zhang et al. [32] proposed two heat release modes to examine their specific impacts on stable and continuous steam production, identifying the convective heat transfer coefficient and local heat flux density during the heat release process. As for solid particle materials, Lai et al. [33] reviewed the thermodynamic properties of various solid particles, identifying the energy storage potential of materials like quartz sand, silica sand, copper slag, and industrial waste. Based on their findings, iron ore particles, with their high heat storage density (270 kJ/kg) and low cost ($110/ton), emerged as the most promising alternative to molten salt for heat storage applications. The sintering process in metallurgical processes generates 30 % ~ 40 % of reclaimed particles, the reuse of which results in additional energy consumption and greenhouse gas emissions. The combination of TES media and the reuse of regrind particles have far-reaching implications for a dual-carbon strategy.

Cogeneration units often face the problem of difficult decoupling of heat and power. A cogeneration unit in southern China needs to supply 150 t/h of high-temperature and high-pressure steam to the surrounding printing and dyeing industry in a stable manner, as shown in Fig. 1. During the valley power period, 50 t/h of reheat steam (cold side) and 100 t/h of reheat steam (hot side) are supplied to the factory via extraction points 1 and 2 respectively. At this time, solid particles absorb the steam energy at extraction point 3 to reduce the unit load. During peak power periods, 100 t/h of reheat steam (hot end) is supplied to the plant via extraction point 1. Solid particle energy release supplies the remaining 50 t/h of steam. The modified unit achieves the dual purpose of thermoelectric decoupling and increased revenue. However, the charging/discharging process between solid particles and steam must be clarified to determine industrialized design parameters.

This study will leverage the iron ore sintering laboratory jointly established by our research team and BHP to explore the feasibility of using iron ore particle-packed beds as heat storage media for steam extraction. These results will provide foundational charging data for different steam extraction points. The discharge capacity will be determined based on the established bed layer temperatures. Additionally, the power generation capacity of beds at different temperatures will be analyzed from various perspectives, including discharge power, efficiency, temperature uniformity within the bed, steam production rate, and quality. Finally, the phase change process during heat release will be elucidated by analyzing the device's temperature and temperature difference maps. Heat release mechanisms at different bed layer temperatures were investigated, and the migration rate of the phase change region (PCR) was derived. The experimental data will confirm the feasibility of steam extraction and storage in solid particles for power plants, providing a research basis for predicting the rate and capacity of heat storage and release processes for load variation in thermal power flexibility retrofit.

2. Experimental introduction

2.1. Experimental setup

As shown in Fig. 2, the system is divided into two main parts: the experimental platform and data acquisition. The experimental platform comprises a soft water tank, pump, fuel boiler, superheater, steam storage tank, TES, and water pool. Two valves and three flowmeters control and measure steam and water flow rates. The data acquisition system consists of a computer and a data acquisition card, which records

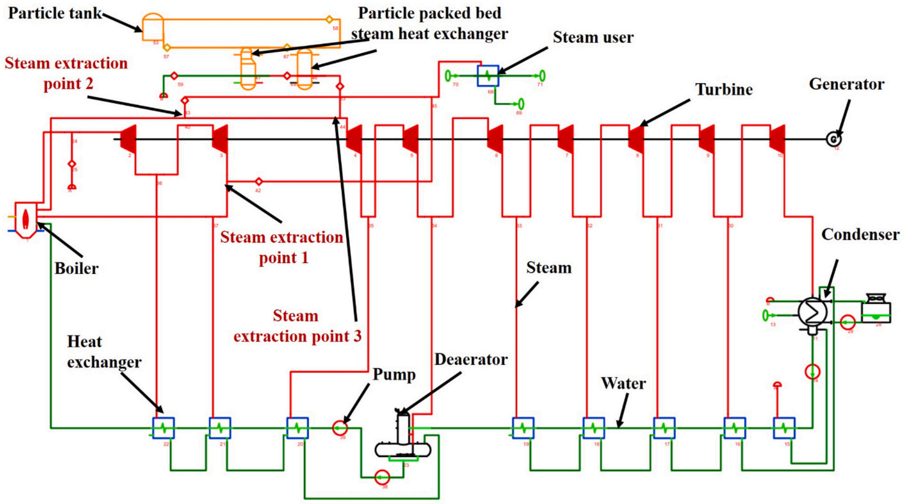

(a) Cogeneration plant valley power period - supply steam + pumped steam storage

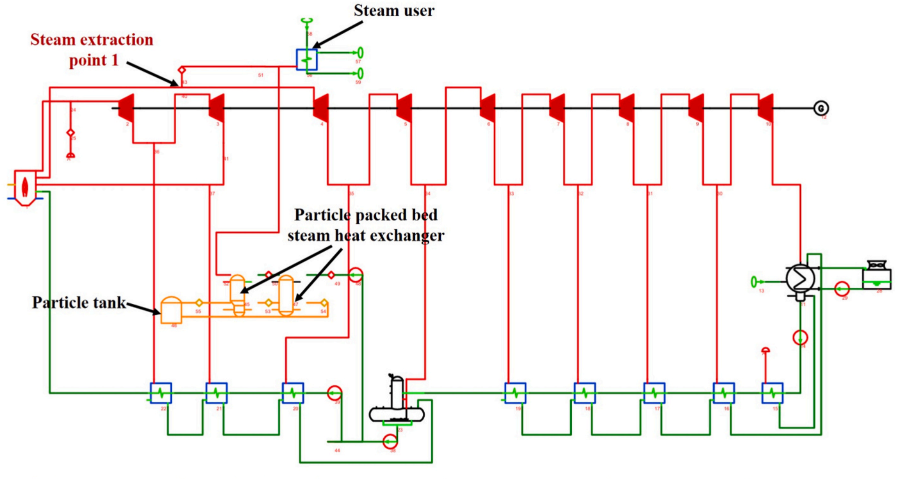

(b) Cogeneration plant peak power periods - energy release to supply steam

Fig. 1. Retrofit program for a cogeneration unit in southern China: heat balance calculation for a unit coupled with solid particle energy storage.

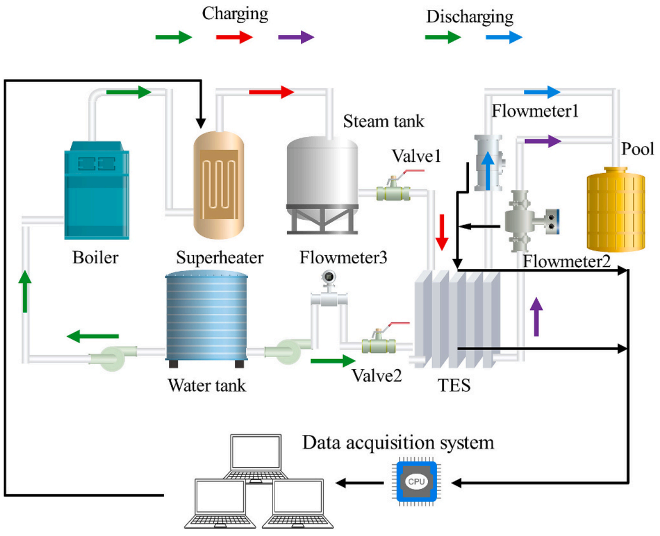

Fig. 2. The experimental system and procedure.

temperature, flow rate, and pressure data. Additionally, the computer regulates the power of the superheater to achieve the operating steam temperature. The internal structure of the TES is illustrated in Fig. 3, with (a) depicting the operational state of the TES. Externally, the device is enclosed by insulation material and an aluminum alloy casing. The pipes above the device are wrapped with insulation cotton, with the black valve corresponding to valve 1 in Fig. 3(b), and (c) presenting the front and top views of the internal structure of the TES. There are a total of 10 layers of coils, with each layer containing two pipelines connected by U-shaped tubes. Fifty thermocouples are arranged in the middle of the U-shaped tubes to detect the temperature of the surrounding solid particles. In addition, the inner diameter of the coil was 26 mm, and the length of each layer of the coil bundle was 912 mm, with 108 mm and 76 mm spacing between coil bundles on each piece and layer. H-type fins, with a thickness of 2 mm, are arranged around the coils, with the length and height being 64 mm each. Please refer to the paper [34] from our research group for further dimensions. The particle size distribution, porosity, and thermal storage parameters of the particle bed formed by natural accumulation are shown in Table 1. Device contains reclaimed ore particles covering all coils as shown in Table 2, mainly 67 % Fe_2O_3 and 17 % CaO. Ultimately, it was confirmed that the entire device was filled with 216 kg of 0–2 mm reclaimed ore particles after weighing.

Table 1
Physical properties of RF particles and the bed accumulation.

Accumulative properties		Physical properties	
Equivalent pore diameter um	Percentage %	Thermal property parameters	Value
>75	27	Cp (20–380 °C)	0.67–0.97 kJ/kg·K
30–75	5	ρ_a (apparent density)	3872 Kg/m^3
5–30	16	ρ_b (bulk density)	2384 Kg/m^3
0.1–5	43	ε (porosity)	0.384
<0.1	9	Thermal conductivity	1.51 W/m·K

2.2. *Experimental conditions and procedures*

The current study investigates the charging characteristics at different steam temperatures and the discharging characteristics at different temperature bed layers. Considering the steam temperatures in power plants and experimental safety, we selected four charging temperatures: 250, 300, 350, and 400 °C. At each charging temperature, a temperature rise of 100 °C in the solid particle-packed bed is achieved to horizontally compare charging efficiency and other parameters. Four temperature bed layers finally formed will be subjected to the same subcooling water flow rate to compare the discharge potential horizontally. The specific operating conditions are listed in Table 3. In addition to the important temperature factor, several other aspects warrant further investigation, including optimal charging strategy selection, cycle charging and discharging, stress field distribution during the charging process, and stepwise charging modes. Considering the timeliness of the research and the already excessive length of this manuscript, these research findings will be presented in manuscript form at a later stage. The charging and discharging process of the system is described as follows, taking case 1 as an example:

1. Open the drain valve of the superheater and steam tank, and start the fuel boiler for steam purging to remove condensate;
2. Close the drain valve and open valve 1 for preheating. Stop preheating when the temperature of the packed bed tends to 150 °C;
3. Set the outlet temperature of the superheater to 250 °C and begin charging until the temperature inside the device stabilizes at 250 °C, completing the charging process;

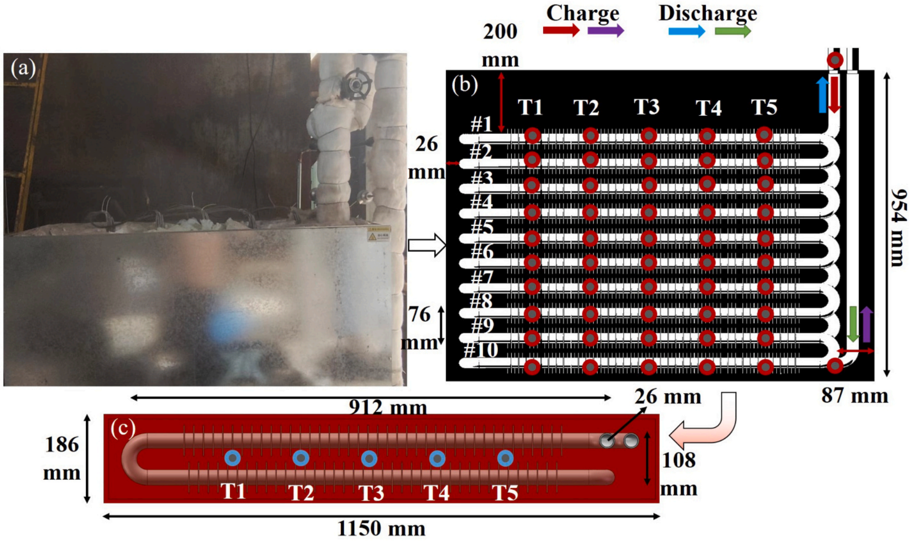

Fig. 3. Internal structure and on-site diagram of the TES device.

Table 2
The composition and element analysis of the return fine particle.

XRF analysis of return fines													
Oxide	MgO	Al_2O_3	SiO_2	P_2O_5	SO_3	Cl	K_2O	CaO	TiO_2	MnO	Fe_2O_3	SrO	–
wt (%)	6.069	2.466	5.754	0.194	1.02	0.038	0.076	17.021	0.13	0.206	66.981	0.044	–

XRF analysis of return fines													
Element	O	Mg	Al	Si	P	S	Cl	K	Ca	Ti	Mn	Fe	Sr
wt (%)	30.222	3.131	1.538	2.549	0.081	0.391	0.036	0.063	11.96	0.078	0.166	49.742	0.042

Table 3
Experimental conditions and other fundamental parameters.

Case	Charging temperature/Range °C	Charging flow rate Kg/h	Bed layer temperature °C	Discharging flow rate Kg/h	Discharging temperature °C
1	250/(150–250)	300	250	50	15
2	300/(200–300)		300		
3	350/(250–350)		350		
4	400/(300–400)		400		

(4) Close valve 1, open valve 2 and start water pump to inject subcooling water into the device for discharging;
(5) Close valve 2 and the water pump when the reading of flowmeter 1 reaches 0, ending the discharge process.

2.3. Data acquisition

Temperature data are collected using Agilent DAQ cards, while flow and pressure values are transmitted using the RS485. Range and accuracy of the thermometers and flowmeters are as follows: 0–1100 °C, ±1 °C and 20–400 kg/h, 1.5 %.

2.4. Mathematical model

2.4.1. Charging process

Charging power is an important indicator characterizing the peak shaving rate of TES. Eq. (1) calculates the charging power by computing the enthalpy drop between the steam inlet and outlet.

$$Pc = mg,c\left(H_{\text{in,c}}\left(T_{\text{in,c}}, Pr_{\text{in,c}}\right) - H_{\text{out,c}}\left(T_{\text{out,c}}, Pr_{\text{out,c}}\right)\right) \tag{1}$$

The overall convective heat transfer coefficient K of the TES is an essential indicator of the device's heat transfer capability, reflecting both the structure of the heat exchanger and the heat absorption capacity of the energy storage material. According to the research by Lv et al. [35], K of the TES is calculated using Eq. (2). *T1(#2)* and *T1(#10)* represent the temperatures of solid particles at the corresponding positions; A represents the heat exchange area of the device, m^2.

$$K = \frac{Pc}{A \times \frac{\left(T_{\text{in,c}} - T1(\#2)\right) - \left(T_{\text{out,c}} - T1(\#10)\right)}{ln\left[\left(T_{\text{in,c}} - T1(\#2)\right) / \left(T_{\text{out,c}} - T1(\#10)\right)\right]}} \tag{2}$$

Thermal resistance reflects the heat absorption resistance of heat transfer exchangers and energy storage media. Heat transfer tubes and fins are considered whole and ignore the contact resistance. Eq. (3) provides the calculation method for total thermal resistance. Eqs. (4) and (5) were used to calculate the convective term of the charging steam. The Nu is calculated by Eq. (5) of the Gnielinski equation [36]. The tube wall thermal resistance is determined using Eq. (6), with the carbon steel's thermal conductivity being 40 W/(m·K). Conversely, the solid particle thermal resistance cannot be directly measured and must be calculated using Eq. (7).

$$\frac{1}{K} = R_{\text{HTF}} + \frac{R_{\text{wall}} \times R_{\text{fin}}}{R_{\text{wall}} + R_{\text{fin}}} + R_{\text{S}} \tag{3}$$

$$R_{\text{HTF}} = \frac{D_{\text{inner}}}{Nu\lambda_{\text{HTF}}} \tag{4}$$

$$Nu = \frac{(f/8)(Re - 1000)Pr}{1 + 12.7\sqrt{f/8}\left(Pr^{2/3} - 1\right)}, f = (1.8\text{lgRe} - 1.5)^{-2} \tag{5}$$

$$R_{\text{wall}} = \frac{ln\left(D_{\text{outter}}/D_{\text{inner}}\right) \times D_{\text{outter}}}{\lambda_{\text{wall}}} \tag{6}$$

$$R_{\text{S}} = \frac{l_{\text{S}}}{\lambda_{\text{S}}} + \frac{1}{h_{\text{S,conv}}} = \frac{1}{K} - R_{\text{HTF}} - \frac{R_{\text{wall}} \times R_{\text{fin}}}{R_{\text{wall}} + R_{\text{fin}}} \tag{7}$$

Two efficiency metrics are proposed for the charging process to represent the energy conversion capacity of the system. Instantaneous charging efficiency (η_r) indicates the ratio of heat absorbed by solid particles to heat released by steam at a specific moment, varying over time. Overall charging efficiency (η_c) represents the ratio of energy absorbed by solid particles to energy released by steam throughout the charging process.

$$\eta\text{r} = \frac{Pc(t)}{\text{M}\Delta T(t)Cp(t)} \tag{8}$$

$$\eta_{\text{c}} = \frac{Qc}{E_{\text{c}}} = \frac{\text{M}\left(T_{2,\text{c}} - T_{1,\text{c}}\right)\overline{Cp'}}{\int_0^{t'} Pc \cdot dt} \tag{9}$$

2.4.2. Discharging process

Discharge power is an important indicator reflecting the peak rate of the TES. Eq. (10) uses the enthalpy rise of the inlet and outlet media to represent the supply rate of the TES discharging process. Discharge efficiency (η_d) is a total efficiency metric representing thermal energy transfer from solid particles to steam throughout the entire discharging process, as shown in Eq. (11).

$$Pd = mg,\text{d}(Hin,\text{d}(Tin,\text{d},Pin,\text{d}) - Hout,\text{d}(Tout,\text{d},Pout,\text{d})) \tag{10}$$

$$\eta_{\text{d}} = \frac{Ed}{Qd} = \frac{\int_0^{t''} Pd \cdot dt}{\text{M}\left(T_{2,\text{c}} - T_{3,\text{d}}\right)\overline{Cp''}} \tag{11}$$

MATLAB R2021b was utilized to generate ΔT distribution cloud map within the packed bed to describe the path of the PCR in the discharge process. Coordinates X and Y and of the PCR at various times were determined to quantitatively analyze the evolution of these regions, as represented by Eq. (12) [37].

$$\overline{X} = \frac{\sum_{i=1}^{N} xi}{N} \qquad \overline{Y} = \frac{\sum_{i=1}^{N} yi}{N} \tag{12}$$

2.4.3. Uncertainty analysis

In addition to directly measured parameters such as temperature and flow rate, the uncertainty of indirectly measured parameters like power is determined by Eq. (13).

$$\frac{\Delta N}{N} = \frac{1}{N}\sqrt{\left(\frac{\partial f}{\partial x}\right)^2 \Delta_x^2 + \left(\frac{\partial f}{\partial y}\right)^2 \Delta_y^2 + \left(\frac{\partial f}{\partial z}\right)^2 \Delta_z{}^2} \tag{13}$$

3. Results and discussion

3.1. Comparison of charge properties at different steam temperatures

Fig. 4 illustrates the vertical temperature evolution within the TES under four charging temperatures, using 10 temperature measurement points inside T3 holes for analysis. Solid particles near each measurement point are sequentially heated along the direction of steam flow, decreasing overall temperature distribution from #10 to #1. Two important points need to be clarified: (1) Due to the high density of reclaimed ore particles, the bottom-most layer #1 comes into contact with the device's outer shell, leading to temperature measurement deviations. (2) The top temperature of the device is the highest and subjected to natural convection from the external air. Therefore, at certain times, the temperature of #10 may be lower than that of #9. Taking (c) as an example, the temperature rise within the TES is extremely slow during the later stages of charging due to the continuously shrinking temperature difference. Considering the time cost, the charging process is halted when the solid particles reach approximately 90 °C higher than their initial temperature for all four charging temperatures. It can be observed that the charging time for 350 °C reaches 105 min, while for the other three temperatures, it's approximately 80 min each. Since steam enters from the top, the solid particles in the upper layers of the device tend to stabilize first (no longer rapidly increasing). The duration from when the temperature at measurement points stabilizes to the end of charging is the main cause of temperature differences between solid particles in the bed layers. The longer this period, the smaller the differences between adjacent bed layers. At the end of charging, the temperature differences between bed layers continuously increase from the top to the bottom of the device, rising from about 1 °C to 5 °C/78 mm.

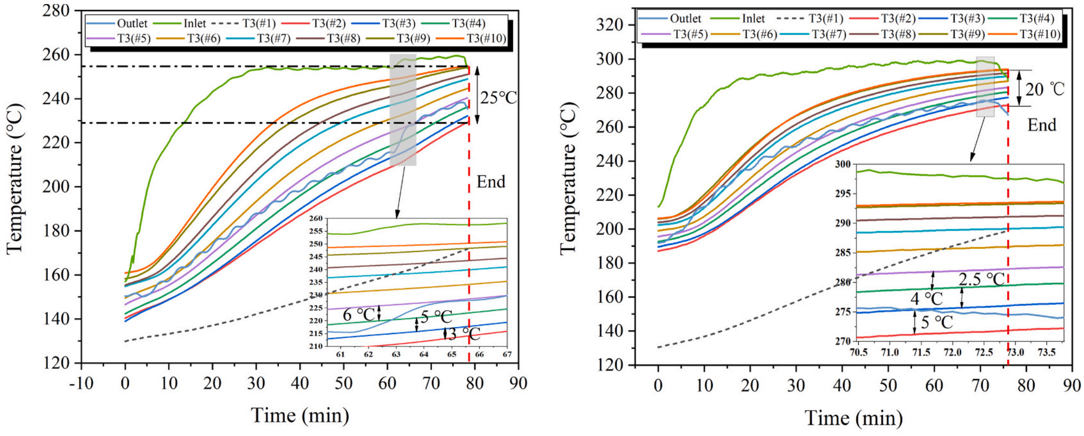

(a) Charge temperature 250 ℃

(b) Charge temperature 300 ℃

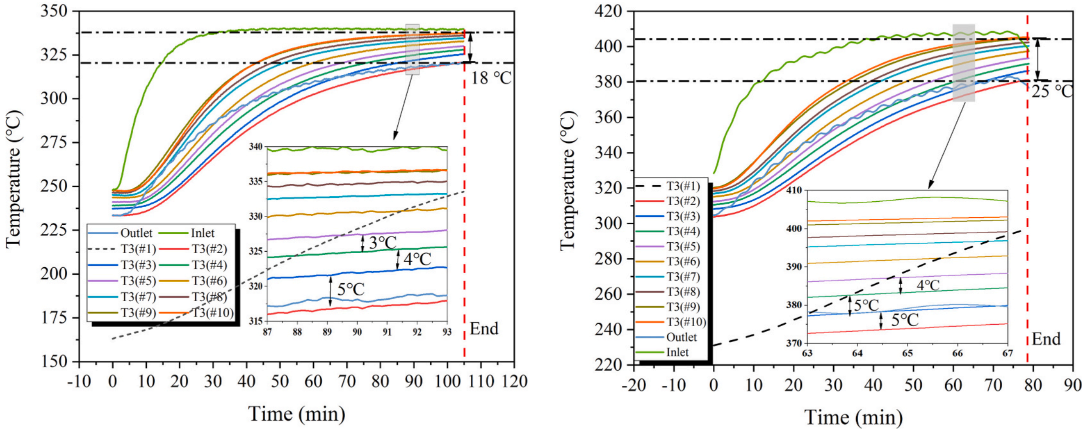

(c) Charge temperature 350 ℃

(d) Charge temperature 400 ℃

Fig. 4. Vertical temperature distribution in the bed during the charging process: Taking the T3 temperature measurement point as an example.

The abnormal temperature difference in the bed layers corresponding to the charging temperature of 250 °C may be due to the shorter charging time, as the overall temperature of the bed layers has not yet fully stabilized, which can be seen from the slope of the temperature curves of each measurement point at the end of charging and the total temperature difference of 25 °C. Overall, the charging temperature has little effect on the charging time, but Fig. 5 shows that it does have a certain impact on the temperature differences between bed layers.

Flow field uniformity is crucial for TES systems using molten salt, as maldistribution can significantly impact their performance. Correspondingly, temperature field uniformity is a key parameter for solid particle-packed beds and requires careful investigation. At 250 °C, Fig. 5 shows that the temperature difference between bed layers is most pronounced, reaching 50 °C. In contrast, the temperature difference is only 30 °C for the other three charging temperatures, consistent with the bed layer temperature curves in Fig. 4(a). Fig. 6 shows the temperature variation trend at the same horizontal level of the device with different charging temperatures. Consistent with previous conclusions, the horizontal temperature differences are generally within 5 °C. The horizontal temperature ranking for 250 °C is: T1 > T5 > T4 > T3 > T2, for 300 °C is: T1 > T4 > T5 > T3 > T2, for 350 °C is: T1 > T5 > T3 > T2 > T4, and for 400 °C is: T1 > T4 > T5 > T3 > T2. It can be observed that solid particles near the bend pipe are easier to heat compared to those inside due to a bigger heat area, which is consistent with the phenomenon that the bend pipe is mostly in the PCR. Reduction in flow velocity and turbulence caused by the bent pipe are the main means of enhancing heat transfer. Although there is no significant difference in the temperature distribution within the bed layers for different charging temperatures, there are differences in the corresponding charging power and cumulative energy.

As shown in Fig. 7(a), 250 °C exhibits the highest charging power, reaching approximately 10 kW, followed by 400 °C, 350 °C, and 300 °C. Taking the average charging power from 10 to 60 min as an example, at 250 °C, it is 7.42 kW (relative error: ±2.6 %), while at 300 °C, 350 °C, and 400 °C, it is 5.1 kW (±2.1 %), 5.48 kW (±2.2 %), and 5.67 kW (±2.2 %), respectively. The difference in charging power between 300 °C and 400 °C is small, but there are differences in the time required to reach the same cumulative energy. Using 20 MJ as a benchmark, the time for 250 °C is 42.5 min, while for 400 °C, 350 °C, and 300 °C, the corresponding times are 59, 62.5, and 65 min, respectively. This is a peculiar phenomenon, which is further analyzed in Fig. 8(a). Taking the interval of 10 to 40 min for comparison, the maximum temperature drop at the steam inlet and outlet corresponding to 250 °C can reach up to 70 °C, indicating a strong ability to transfer steam energy into the heat exchanger (including absorption by solid particles and heat loss), which corresponds to its highest charging power. Next are 350 °C, 300 °C, and 400 °C, respectively. Combining the variation curve of charging power in Fig. 7(a), the steam inlet and outlet temperature difference is positively correlated with power. At 10 min, 300 °C corresponds to a higher power and temperature difference. Between 35 and 40 min, the power corresponding to 400 °C exceeds that of 300 °C, and subsequently, the temperature difference curve in Fig. 8(a) also shows a crossover. Although the temperature difference corresponding to 350 °C is significant, the charging power is not significant, mainly due to fluctuations in steam flow resulting in a smaller flow rate at 350 °C.

Fig. 8(b) shows the thermal resistance curve from 10 to 40 min. It can be seen that the thermal resistance of solid particles is the smallest at 250 °C, approximately 0.002 (m^2·K/W), which is consistent with the thermal resistance value on the steam side. The wall thermal resistance is the smallest, approximately 0.00016 (m^2·K/W). The more minor thermal resistance of solid particles comes from two aspects: the low specific heat capacity of solid particles at low temperatures and the smaller temperature difference with the ambient temperature. Furthermore, the thermal resistance on the solid particle side is the largest (0.004 (m^2·K/W)) during charging at 300 °C and 350 °C, then it begins to decrease, reaching 0.003 (m^2·K/W) at 400 °C. The authors

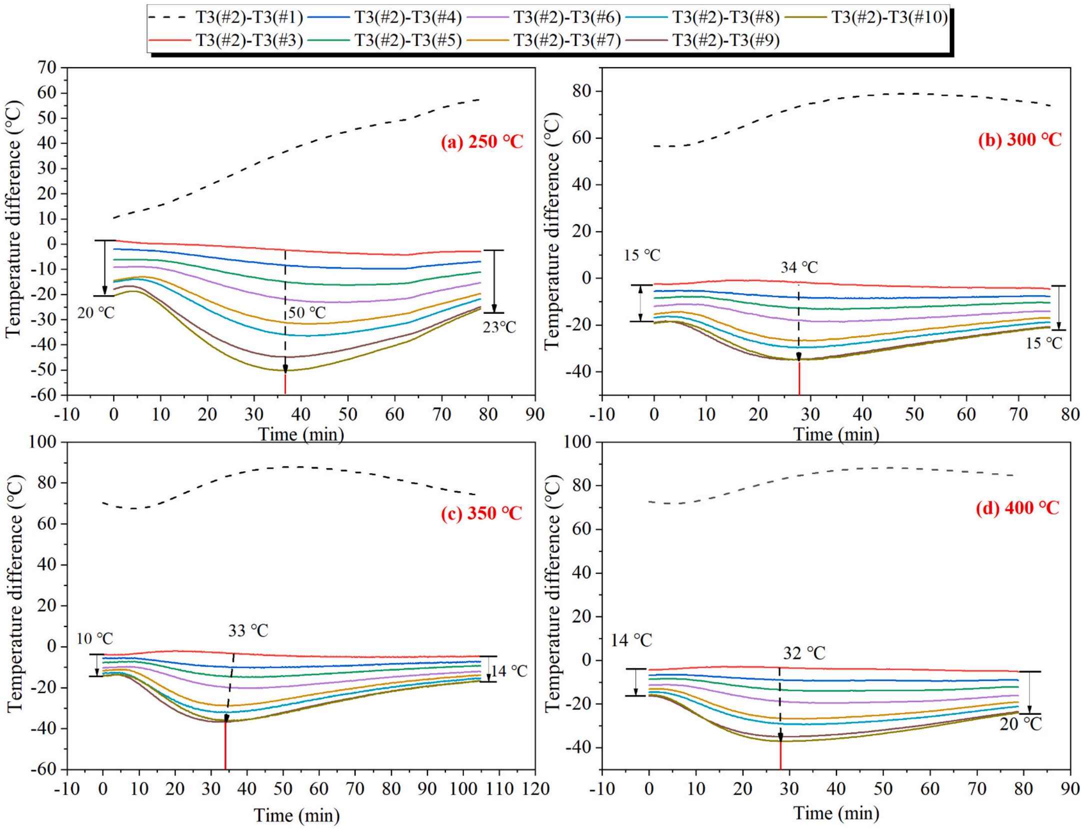

Fig. 5. Temperature difference in the vertical direction of the bed during the charging process: A case study using the T3 temperature measurement point.

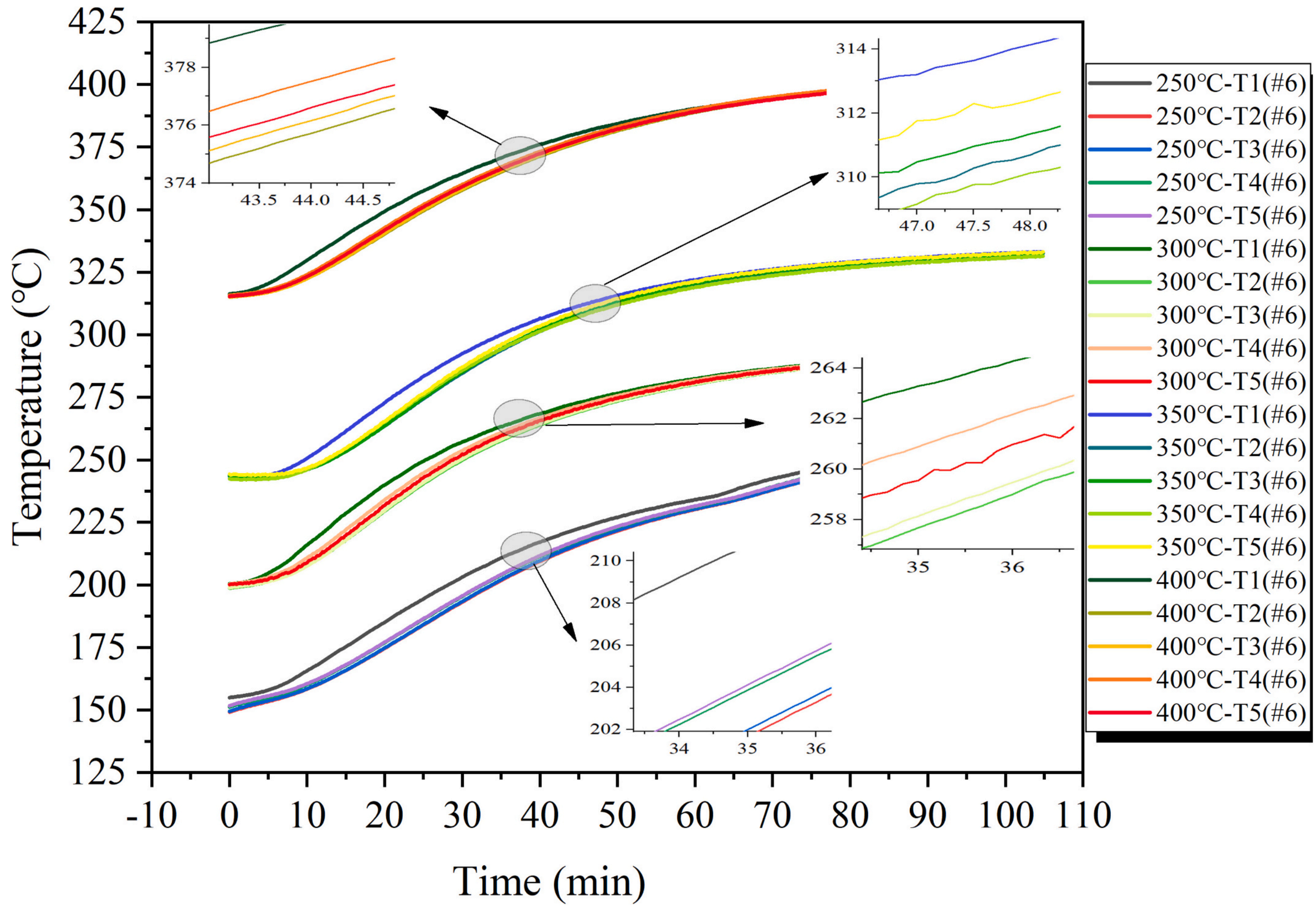

Fig. 6. Horizontal temperature differences in the bed corresponding to different charging temperatures: A case study using temperature measurement point #6.

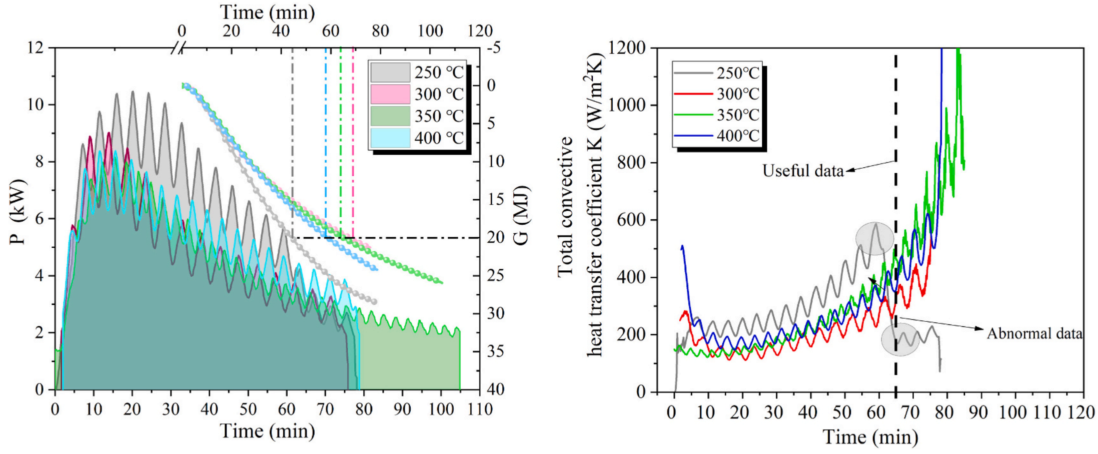

(a) Charging power and accumulated energy

(b) Convective heat transfer coefficient

Fig. 7. Power, energy, and convective heat transfer coefficient at different charging flow rates.

believe the intensified air thermal convection within the solid bed increases the thermal conductivity, resulting in smaller thermal resistance and higher charging power at 400 °C. Fig. 7(b) illustrates the trend of convective heat transfer coefficients for the four temperatures. Due to the large steam flow required for system charging, the temperature is difficult to rise to the target quickly. The system is unstable during this period, so the data for the first 10 min before charging begins are not representative. Similarly, the convective heat transfer coefficient

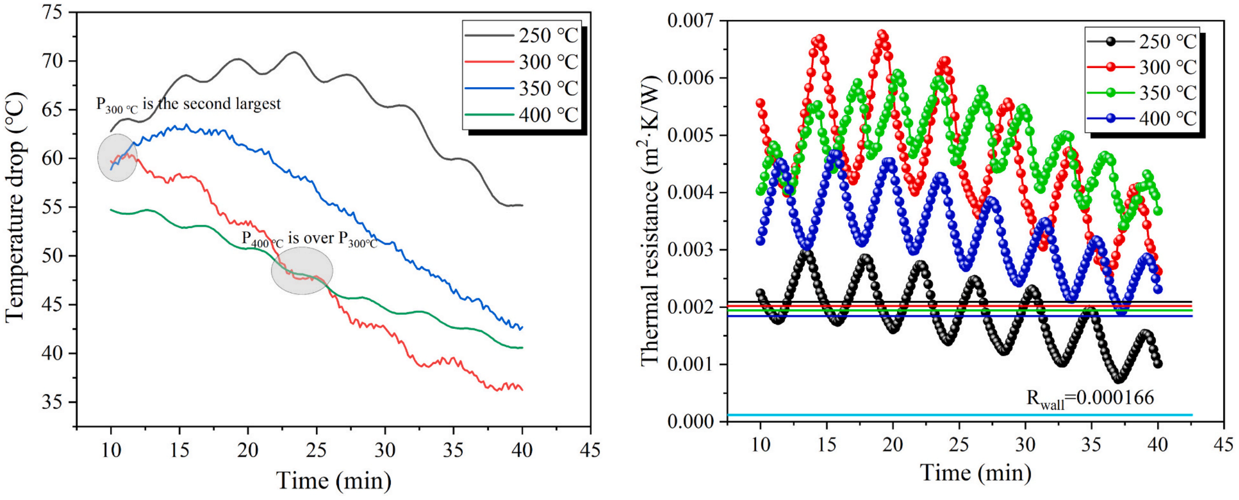

(a) Temperature drop of steam

(b) Thermal resistance

Fig. 8. Steam temperature drop during the charging process at different temperatures and the thermal resistance of the accumulated bed.

increases linearly because the temperature differences between steam and solid particles are close to zero before the charging ends. Therefore, the convective heat transfer data in the late-charging stage are also not representative. The authors selected data from 10 to 60 min for comparison. It can be observed that 250 °C has the highest convective heat transfer coefficient, approximately 314.37 W/(m^2·K) (relative error: ±3.8 %), followed by 400 °C at approximately 222.91 W/(m^2·K) (±2.9 %), while the convective heat transfer coefficients for 300 °C and 350 °C are similar. This trend is consistent with the results in Fig. 8(b), where lower charging temperatures correspond to smaller particle-specific heat capacity and better charging capability against the reverse environment. The phenomenon of thermal buoyancy induced by the highest charging temperature reduces the thermal resistance of the bed, facilitating heat transfer.

Fig. 9 illustrates the trend of real-time charging efficiency corresponding to temperatures, with data from 10 to 60 min selected for comparison. The real-time charging efficiency at 250 °C is the lowest reaching only about 60 %, and changes more gradually compared to other temperatures. The low real-time efficiency can be attributed to two main reasons: (1) At 250 °C, the thermal resistance of solid particles is low, facilitating the release of a large amount of heat by steam. (2) The specific heat capacity of iron ore particles increases rapidly with temperature, causing even if the same temperature difference is achieved by steam heating the solids, the energy possessed by the lower-temperature solid particles remains at a disadvantage. These two factors cause the denominator to increase while the numerator decreases, ultimately resulting in the lowest real-time efficiency. The maximum real-time efficiency for all four charging temperatures occurs at around 30 min, consistent with Fig. 5, indicating that improved temperature uniformity leads to reduced charging efficiency. Real-time efficiency variation for temperatures between 300–400 °C shows a significant but similar range, primarily due to the lower specific heat capacity of particles in the low-temperature region, resulting in lower thermal inertia. However, particles have a larger specific heat capacity in the high-temperature region, leading to greater thermal inertia. Overall, utilizing the high-temperature segment of iron ore particles for energy storage offers both high energy storage density and reasonable thermal inertia (not significantly exceeding 100 %), thereby maintaining strong thermal responsiveness in the system. Considering multiple indicators such as real-time efficiency, charging time, temperature uniformity, charging power, and convective heat transfer coefficient, charging at 400 °C currently demonstrates significant advantages.

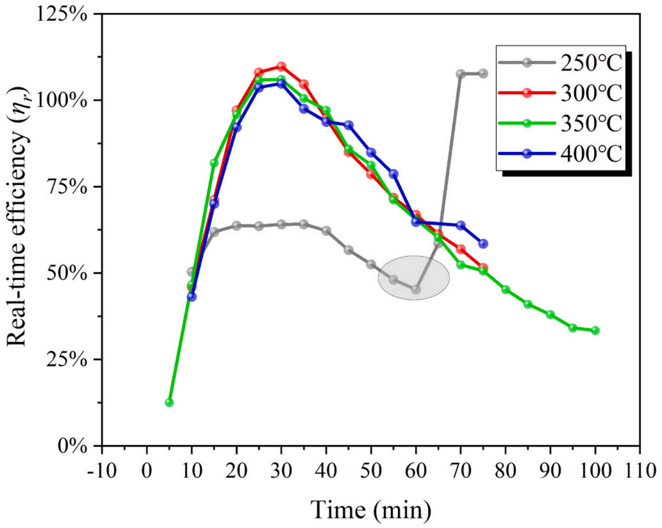

Fig. 9. Trend of real-time efficiency variations corresponding to different charging temperatures.

3.2. *Comparison of discharge properties at different bed temperatures*

Fig. 10 depicts the vertical temperature evolution of bed layers at four different temperatures. The entire process is categorized into three stages based on the stability and continuity of steam output from the system: initial, stable, and exhaustion. In the initial stage, temperature decline is insignificant, with only a slight decrease observed in a few thermocouples at the bottom. During the stable stage, internal temperatures of the bed layers begin to decrease sharply. Considering the discharge process involves three states: single-phase (subcooled water), two-phase (vapor-liquid mixture), and single-phase (superheated steam), the bed layer experiencing the most pronounced temperature decrease is expected to undergo the highest heat absorption during phase change. While the bed layer with a gradual temperature change primarily serves for preheating and superheating purposes. Comparing the temperature measurement points #2, #3, #4, and #5 within the 250 °C bed layer reveals discontinuous phase change phenomena, as observed in previous studies. Similarly, such phenomena are observed at

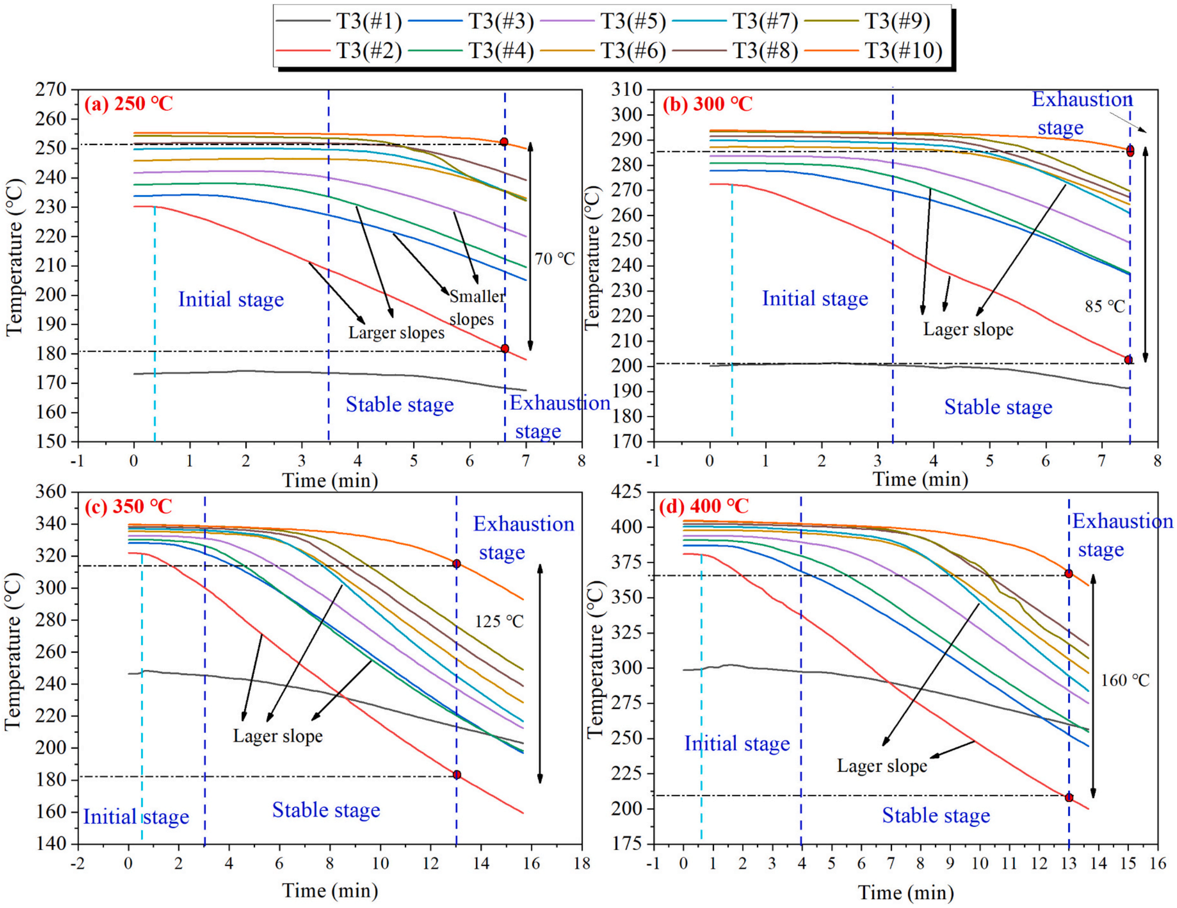

Fig. 10. Vertical temperature distribution in the bed during the discharging process at different temperatures: A case study using the T3 temperature measurement point.

300 °C and 350 °C, where odd-numbered layers of solid particles may correspond to the preheating section, while even-numbered layers correspond to the PCR.

Solid particle beds undergo multiple cycles of charging and discharging for peak shaving in thermal power or mobile heating applications. Therefore, understanding the temperature distribution after heat release is crucial for the next charging cycle. Fig. 11 illustrates the temperature differences among bed layers after heat release (using #2 as the reference). As the bed temperature increases, the temperature difference among particles after heat release becomes larger, with maximum bed temperature differences of 70–160 °C for bed temperatures ranging from 250 to 400 °C, as shown in Figs. 10 and 11. Consistent discharge fluxes but large differences in temperature drop indicate that high-intensity or sustained discharges occur in hotter beds. Despite the smaller temperature differences in the 250 and 300 °C beds, there is an apparent stratification phenomenon. Especially at 300 °C, temperatures at #3, #4, and #5 are similar, significantly lower than those at #6, #7, #8, and #9. There is no apparent stratification at 350 and 400 °C, with consistent temperature-decreasing trends observed across all measurement points. During discharge in high-temperature beds, there may be no distinct preheating, evaporation, or superheating phases. The entering subcooled water is rapidly evaporated over a short distance, causing most regions within the device to be in the evaporation phase. The absence of stratification benefits subsequent charging processes, allowing the system to complete charging quickly without encountering extremely low-temperature regions.

Fig. 12 illustrates the temperature variations at the same horizontal position during discharge at different bed temperatures, with #6 as an example. It can be observed that the temperature at sensor T1 consistently experiences the fastest decrease under all bed temperatures. At 350 °C, a similar phenomenon occurs at sensor T4, indicating the presence of PCR near the bend in the bed layer. Comparing T1 temperature decline trends corresponding to the four different bed temperatures reveals the rate of temperature decline at each sensor continuously decreases as the bed temperature decreases, indicating a weakening of the intensity of phase transition or heat exchange. These data suggest that 350 °C and 400 °C bed layers can produce significant steam flow rates. As shown in Fig. 13, the steam properties generated by the bed layers at different temperatures are provided. Fig. 13(a) illustrates the temperature and pressure variations of the steam produced at 250 °C, while Fig. 13(b) depicts the corresponding trends in flow rate (Qg) and discharge power (P). Similar steam properties for discharge at other bed temperatures are also presented accordingly. Based on the stability and continuity of the steam flow rate in (b), the discharge process is divided into three stages. The steam temperature at the end of the stable stage is defined as the minimum steam production temperature, as indicated by the black arrow in (a). The minimum steam production temperature rises from 205 °C to 275 °C as the bed temperature increases, comparing Fig. 13(a), (c), (e), and (g), which is mainly due to the differences in bed temperature. 250 °C and 400 °C bed layers corresponding to superheated section temperatures are 250 °C and 400 °C, respectively. Furthermore, due to the increased steam production capacity, higher bed temperatures correspond to higher steam pressures, rising from 0.005 MPa to 0.01 MPa. Comparing Fig. 13(b), (d), (f), and (g), it can be observed that as the bed temperature increases, the steam production rate slightly increases, from 26 to 31 kg/h. This indicates that the relationship between steam production rate and bed temperature is not significant, mainly influenced by the flow rate of subcooled

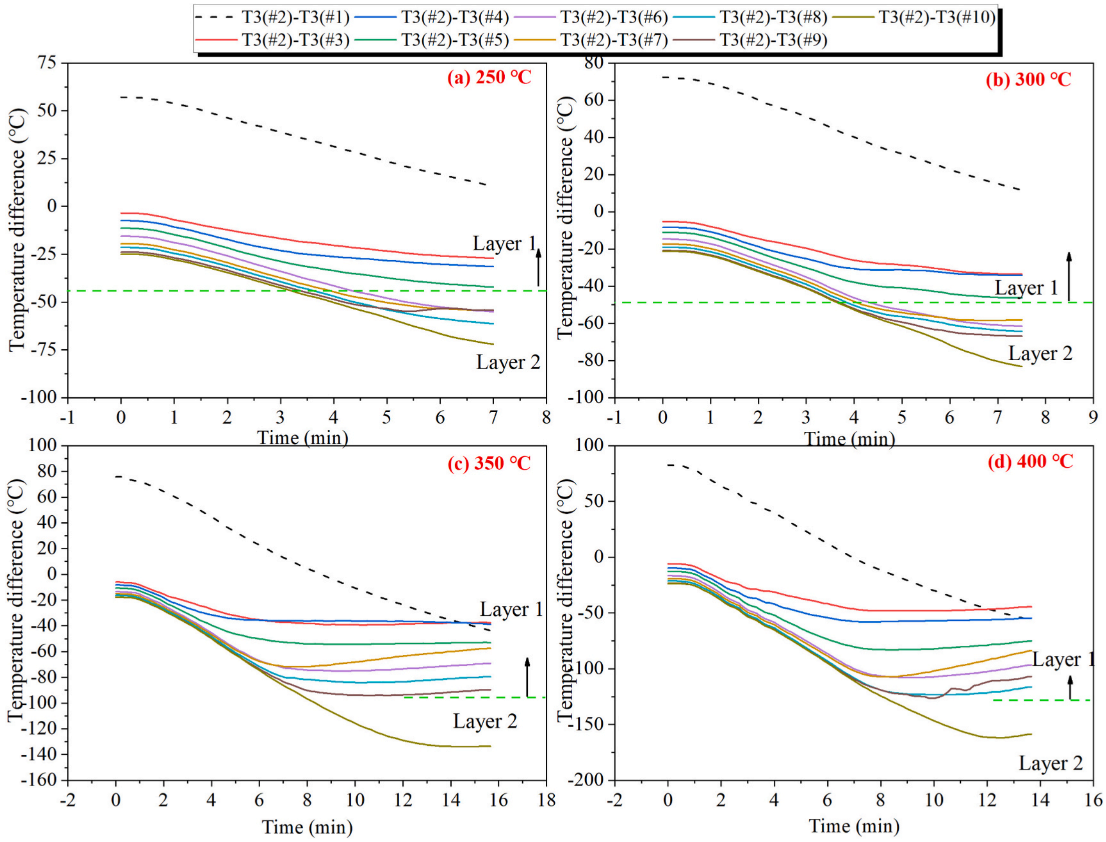

Fig. 11. Temperature difference in the vertical direction of the bed during the discharging process at different temperatures: A case study using the T3 temperature measurement point.

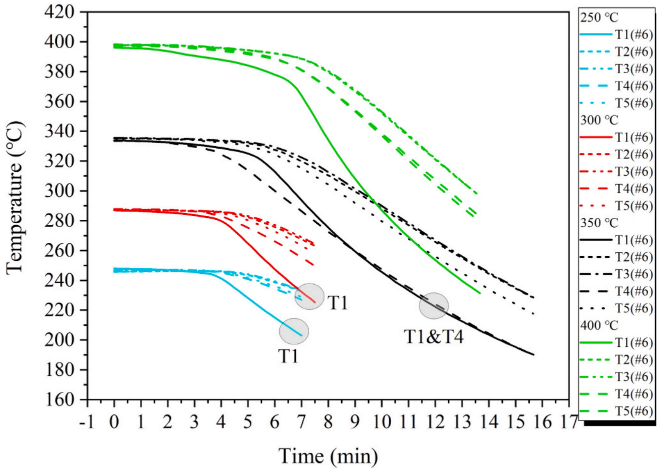

Fig. 12. Horizontal temperature distribution in the bed during the discharging process at different temperatures: A case study using #6 as an example.

water. Consequently, the discharge power also experiences a slight increase with increasing bed temperature, rising from 21 to 31 kW, benefiting from the dual enhancement of flow rate and steam quality. One important point to note is that the device currently cannot produce steam with a stable temperature output. During the discharging process, the internal temperature of the device gradually decreases with the water increases as shown in Fig. 15. Consequently, the superheated zone at the upper part of the device gradually shortens and the temperature of the produced steam also decreases.

Further comparing the continuous steam generation time with the increase in bed temperature, the duration of the stable stage rises from 3 to 9.5 min. Considering the minor differences in steam production rates, the total steam production increases threefold, which is consistent with the bed temperature decreasing. As the bed temperature rises, the extent and intensity of phase transition within the enhanced system ultimately leads to a dual steam quality and quantity enhancement. In summary, at 250 °C bed temperature, a 26 kg/h flow rate can continuously produce overheated steam at 205–220 °C for 3 min. At 400 °C bed temperature, a 31 kg/h flow rate can continuously produce overheated steam at 275–350 °C for 9.5 min. As the bed temperature increases, the stable steam production rate and quality can be significantly enhanced, especially above 350 °C, where this phenomenon becomes particularly pronounced. Therefore, the minimum bed temperature should also be above 350 °C for on-site energy storage and release, which means the extraction steam must be 400 °C in the thermal plant.

3.3. *Efficiency comparison*

Fig. 14 presents the charging and discharging efficiency at different temperatures within the TES. It is observed that the efficiency of steam charging at 250 °C is the lowest, at only 65 %. While at 300 °C, the charging efficiency is highest, at approximately 85 %. The charging efficiency at 350 °C and 400 °C is roughly the same, around 75 %. Although the 250 °C bed has the highest charging power, lower specific heat capacity, and similar temperature rise result in the least heat absorbed by the solid particles, yielding the lowest charging efficiency. On the contrary, there is the lowest charging power at 300 °C, but the solid particle side accumulates a moderate amount of heat under the same temperature rise, resulting in the highest charging efficiency. Therefore, charging efficiency is determined not by the charging power on the steam side but by the heat absorption power on the solid particle side. The highest charging efficiency is achieved when higher heat

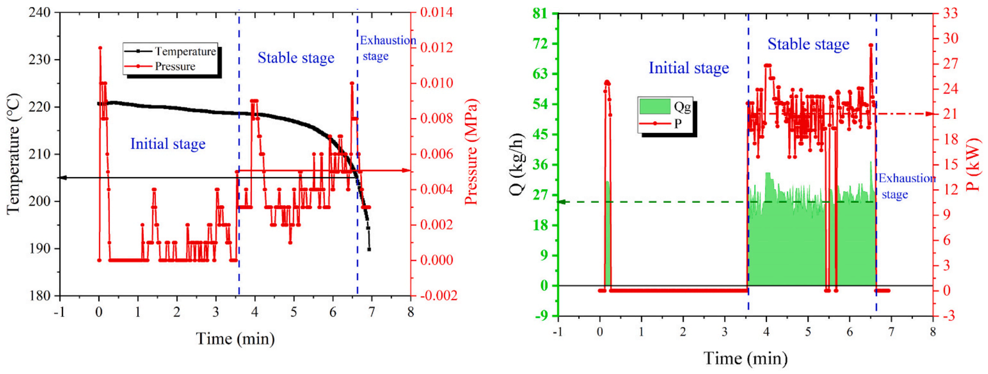

(a) 250℃_Temperature_Pressure (b) 250℃_Qg_P

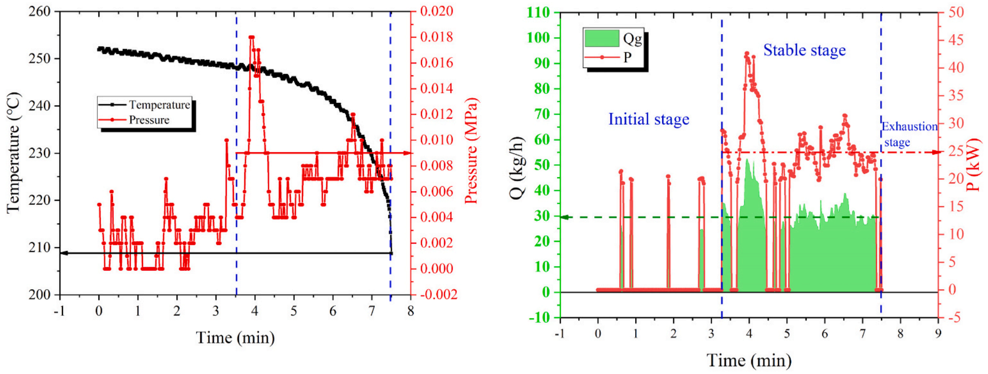

(c) 300℃_Temperature_Pressure (d) 300℃_Qg_P

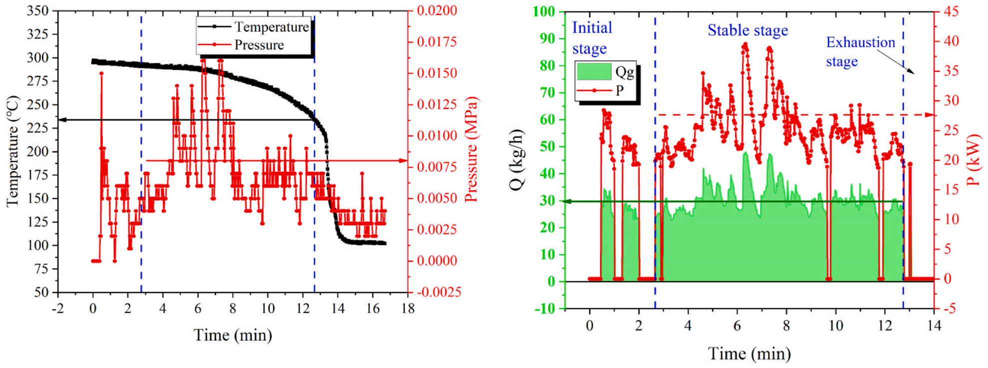

(e) 350℃_Temperature_Pressure (f) 350℃_Qg_P

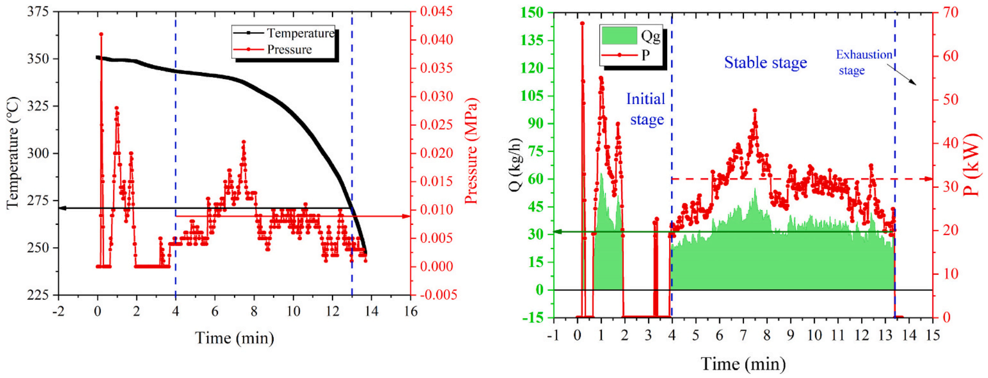

(g) 400℃_Temperature_Pressure (b) 400℃_Qg_P

Fig. 13. Properties of steam generated from bed layers at different temperatures.

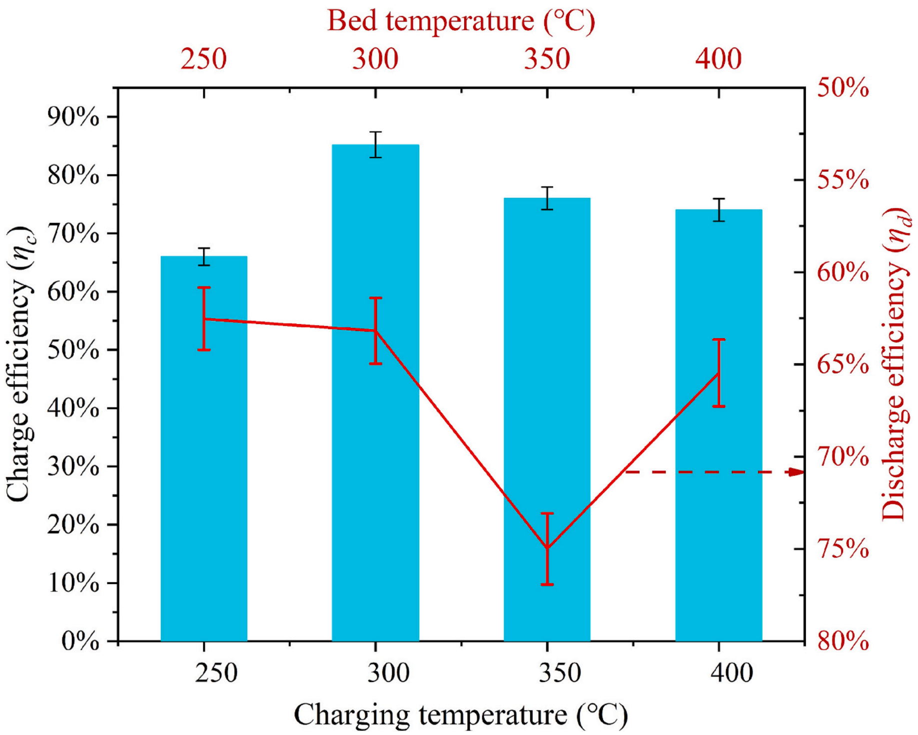

Fig. 14. Charging efficiency of steam at different temperatures and discharging efficiency of bed layers at different temperatures.

absorption power is combined with lower charging power. Additionally, rapid heat absorption on the solid particle side causes a sudden increase in bed temperature, further reducing the temperature difference between steam and solid particles, thereby lowering the charging power. This phenomenon can be verified from Fig. 4, using the average temperature of T3 (#2) to T3 (#10) as the reference. At 300 °C, the bed temperature rises by 50 °C in 28 min, while at 250 °C it takes 34 min, and at 350 °C and 400 °C it takes 32 min. Based on the analysis of discharge process parameters, it can be observed the PCR is extensive and produces a large amount of steam at 350 °C, thus exhibiting the highest discharge efficiency at approximately 75 %. Next is the 400 °C temperature, with an efficiency of approximately 66 %. Efficiencies at 250 °C and 300 °C are lower due to their smaller steam production, at approximately 63 %. 350 °C bed layer has a smaller heat transfer difference than 400 °C, but it also has the ability for rapid evaporation. Compared to the 300 °C bed layer, the 350 °C bed layer has a much broader evaporation section, contributing to its highest discharge efficiency. In summary, it can be concluded that charging temperatures of 350 °C and above may exhibit favorable charging and discharging capabilities from the perspective of charging and discharging efficiency. Furthermore, He et al. [38] showed that the evaporator efficiency of a 300 to 400 °C molten salt steam generation system is roughly 80 to 92 %, and the efficiency of the superheater is 40 to 60 %. The discharge efficiency of the device is slightly lower than that of He et al. Inadequate insulation of the device shell and certain valve pipelines, as evidenced by infrared imaging during the experiment, which revealed noticeable heat dissipation around the connected valve pipelines. In addition, a significant temperature difference between cold water and particles during discharge, resulting in substantial exergy loss.

3.4. *Identification, migration, and mathematical modeling of PCR*

Fig. 15 presents temperature contour maps of the internal discharge process in the packed bed, plotted using data from 50 thermocouple measurements. It can be observed that the area involved in heat exchange within the apparatus expands continuously as discharge time progresses. For temperatures of 250 °C and 300 °C, only contour maps for 400 s are available due to the relatively short duration of the stable phase, whereas for 350 °C and 400 °C, contour maps spanning nearly 900 s are depicted. From the 400 s contour maps corresponding to 250 °C and 300 °C, three distinct regions are discernible within the packed bed: deep blue, light blue, and yellow, corresponding to low-temperature, medium-temperature, and high-temperature regions, respectively. However, it becomes increasingly challenging to generate a stable large quantity of steam at this stage. The authors suggest that the lower bed temperature makes it difficult for the short-distance bed layer to evaporate a significant amount of subcooled water. During the actual heating process, it is challenging to control the maximum bed layer temperature difference within 20 °C, but it must still be higher than the bed layer temperature layout shown in the depletion stage.

Fig. 16 provides temperature difference distribution maps for different discharging processes, plotted based on temperature changes within 10 s. Previous research has identified the preheating, evaporation, and superheating sections within the device through temperature differentials, which will not be reiterated here. Taking 350 °C as an example, the temperature difference within the device is minimal at 0 s, approximately 0.5 °C. As the process progresses, the device begins to encounter subcooled water at 200 s, leading to a significant temperature drop at the bottom, reaching up to 3.5 °C/10 s, primarily distributed at the sides of the device. There is an upward migration of intense cooling regions within the device between 400 and 800 s, with the maximum temperature drop reaching 2.5 °C/10 s. This phenomenon is primarily due to the expansion of the PCR within the device, where localized extensive phase changes are dispersed into widespread minor phase changes. At 940 s, the temperature drop in the middle and lower parts of the device is only 1 °C/10 s. At this point, the middle and lower sections primarily undertake the preheating phase, while phase changes are concentrated mainly in the upper region. Furthermore, a horizontal comparison of the maximum temperature differences in other bed layers reveals the breadth and intensity of the phase change process. At 250 and 300 °C, the maximum temperature drop is only 2.5 °C/10 s, while it reaches 3.5 °C/10 s at 350 °C and 4 °C/10 s at 400 °C. The consistent

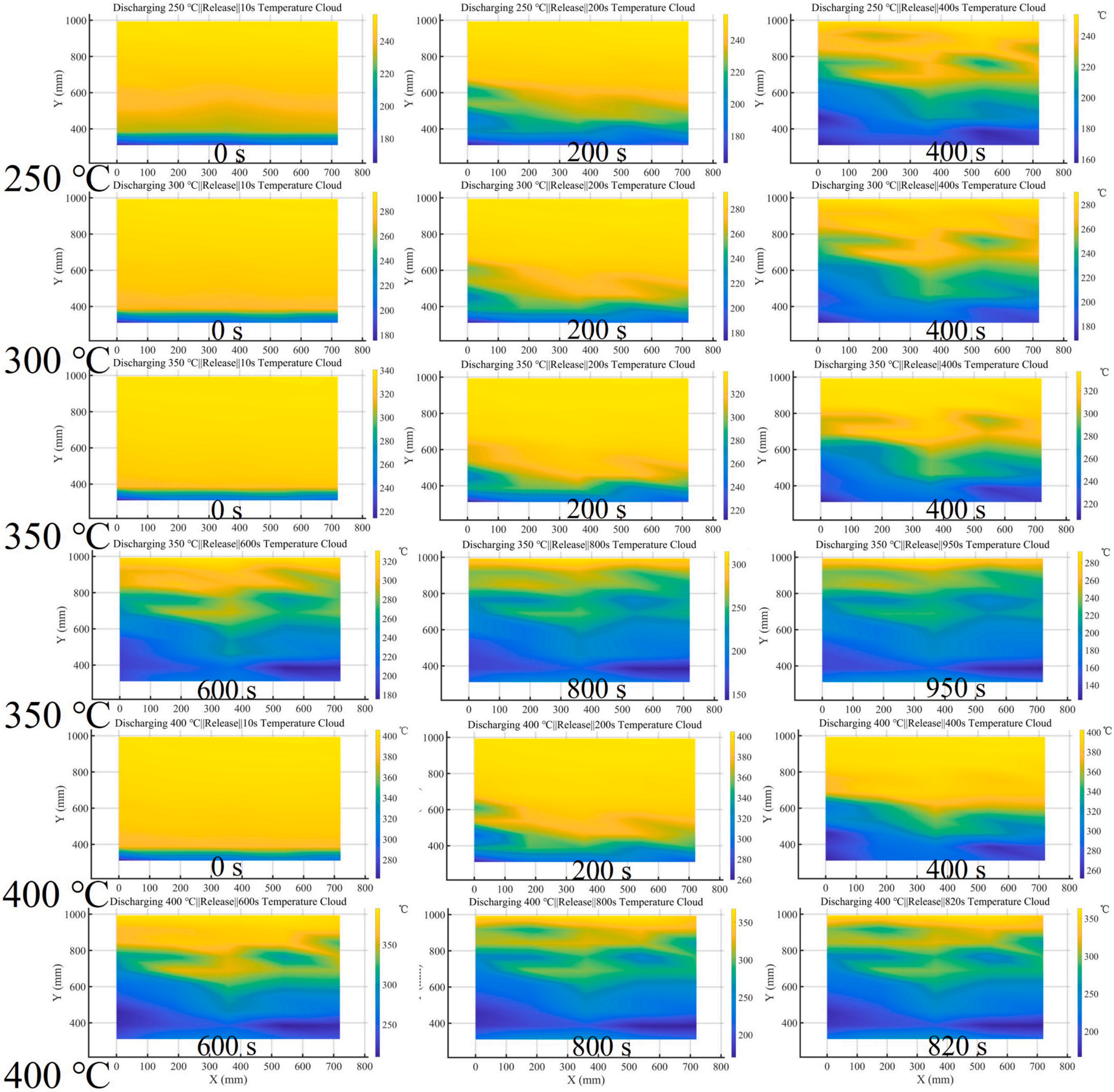

Fig. 15. Internal temperature distribution of the discharging process in bed layers at different temperatures: Using experimental data from 50 thermocouples.

flow rate of the supercooled water resulted in a relatively small difference in maximum temperature drop. Nonetheless, it is still evident that there is the most robust evaporation capability and a more extensive PCR at 400 °C.

To clarify the migration of the PCR within the device, temperature difference cloud maps for each moment were processed using MATLAB 2021b, resulting in the migration curves of the PCR coordinates within the device as depicted in Fig. 17. Temperature drops below −2 °C/10 s were considered significant indicators of phase change in the respective measurement areas based on previous study. The coordinates of these points were recorded, and all recorded coordinates were averaged to obtain the X migration process shown in Fig. 17(a) and the Y migration process depicted in Fig. 17(b) subsequently. As phase change predominantly occurs at the sides of the device, the migration pattern in the X is not distinctly evident, eventually stabilizing at the midpoint of X = 400 mm. It is noteworthy to observe the trend in the Y-direction. As inferred from the previous cloud map analysis [37], the PCR continuously extends upward, as depicted in (b). Migration in the Y exhibits an approximately linear relationship with time. A lower slope indicates slower migration, indicating that the bed energy can sustain phase change for extended periods. Based on the design shown in Fig. 3, temperature data can be converted into the function between the phase transition rate V and t [37]. Final results suggest that the migration speed of the PCR along the tube bundle is around 10–30 mm/s at four different bed temperatures. Flow rate of supercooled water significantly impacts the migration speed of the PCR, while the bed temperature mainly affects the phase transition intensity [37].

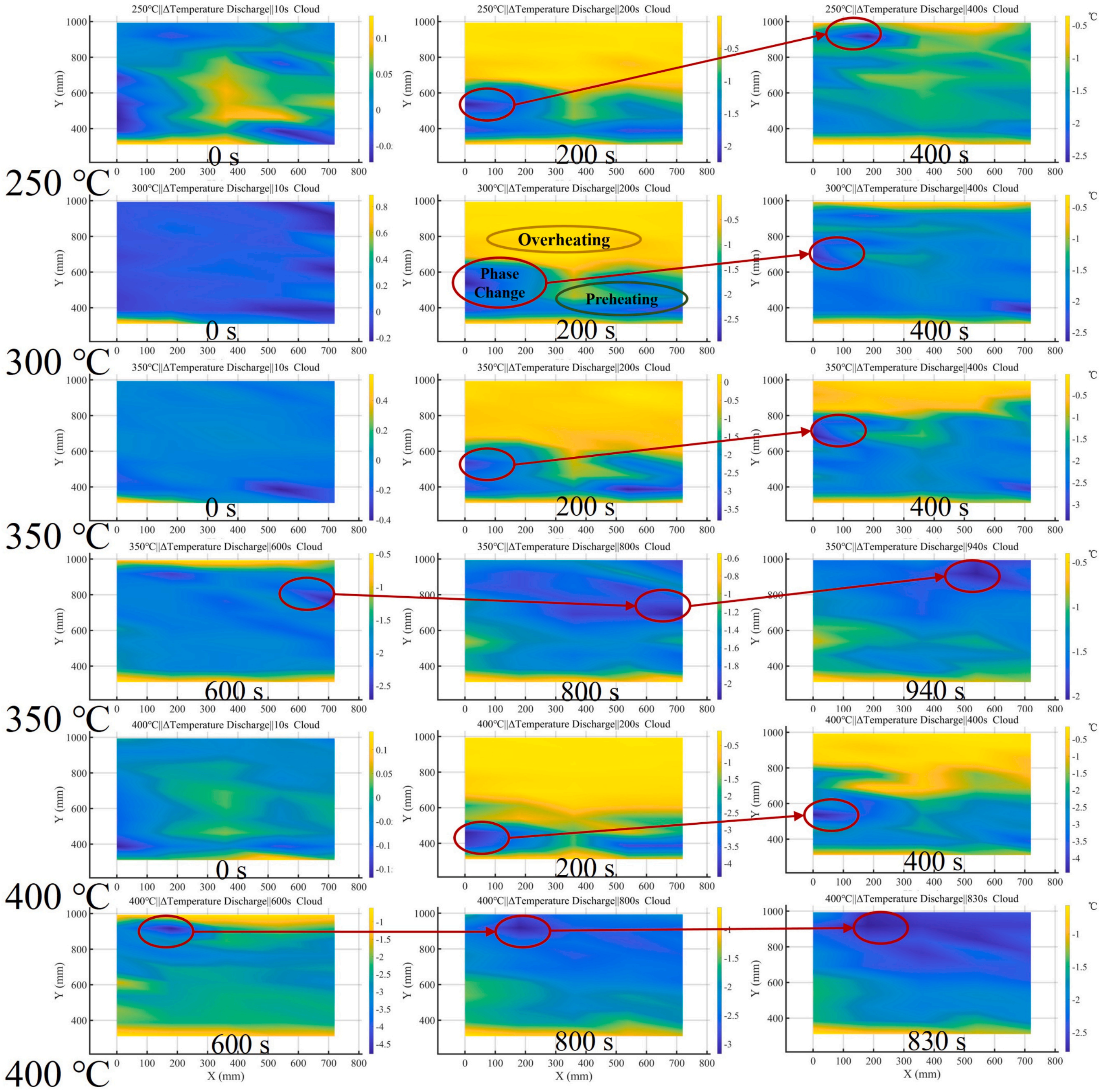

Fig. 16. Thermographic map illustrating the temporal evolution of temperature differentials every 10 s within the apparatus during the discharging process, based on data collected by 50 thermocouple measurements.

$$
\begin{array}{llll}
250^{\circ}C & \overline{Y} = 300 + 1.18t & L = ((300 + 1.18t) - 300)^{*}26.3 & V = dL/dt = 31.0(mm/s) \\
300^{\circ}C & \overline{Y} = 559 + 0.38t & L = ((559 + 0.38t) - 300)^{*}26.3 & V = dL/dt = 10.0(mm/s) \\
350^{\circ}C & \overline{Y} = 335 + 0.67t & L = ((335 + 0.67t) - 300)^{*}26.3 & V = dL/dt = 17.6(mm/s) \\
400^{\circ}C & \overline{Y} = 387 + 0.43t & L = ((387 + 0.43t) - 300)^{*}26.3 & V = dL/dt = 11.3(mm/s)
\end{array}
\tag{14}
$$

During the discharge process, the subcooled water undergoes three stages: preheating (single phase), evaporation (vapor-liquid two-phase), and superheating (single phase). To clarify the influence of bed temperature on the distribution ratio of different phase areas, Eq. (15) for estimating the proportion of each region inside the device is proposed based on the research by Zhang et al. [32]. Due to the prolonged stable steam production capability at 350 and 400 °C, Fig. 18 illustrates the

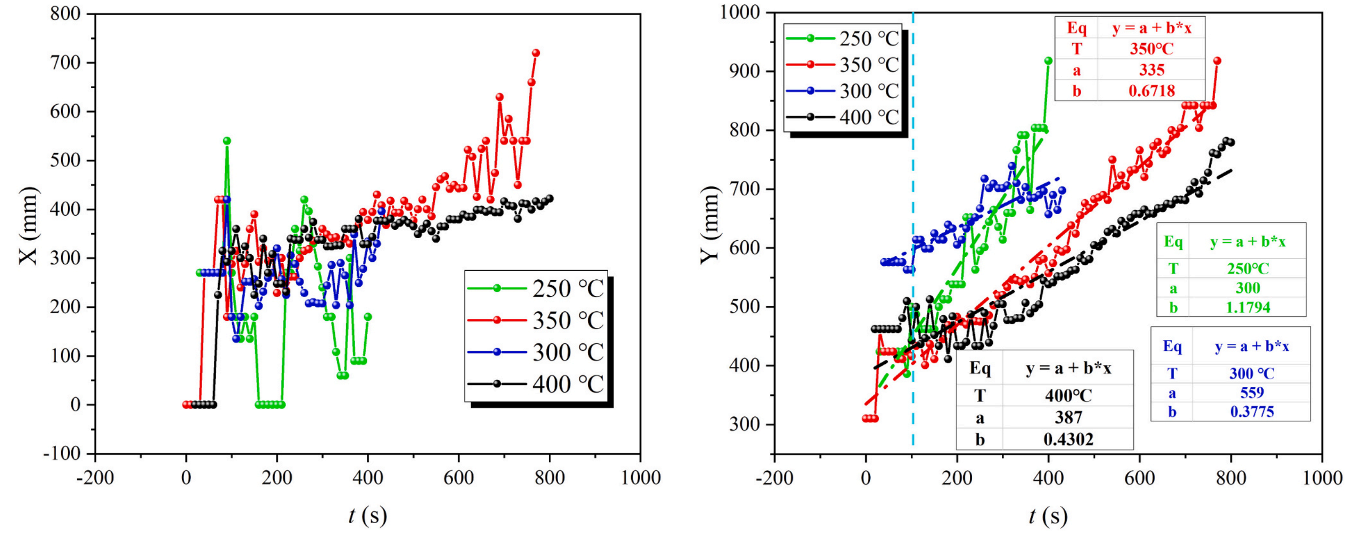

(a) X-direction **(b) Y-direction**

Fig. 17. The process of movement of the PCR in the X and Y directions.

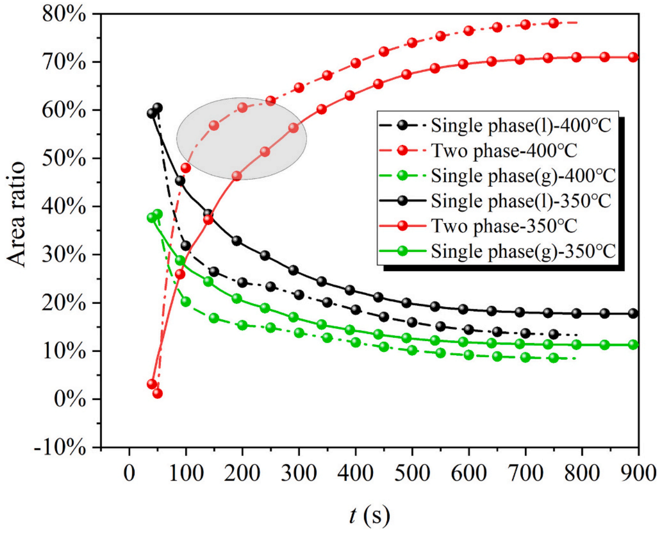

Fig. 18. The proportions of the preheating, evaporation, and superheating sections during the discharging process at 350 and 400 °C.

trends of the proportion changes in various regions during the initial and stable stages at these two temperatures. It can be observed that during the discharge process, the proportion of the gas-liquid two-phase region sharply increases with the increase in inlet water volume (time), while the single-phase region decreases rapidly. The PCR at 400 °C can ultimately occupy 75 % of the device volume, whereas the bed at 350 °C only reaches 65 %. Another difference lies in the intensity of the phase change. The rate of increase in the proportion of the gas-liquid two-phase region within the shaded area indicates the enhancement of the phase change intensity at 400 °C. When entering the depletion stage, the superheated section only occupies 10–20 % of the area, which also reveals the reason for the rapid decrease in steam temperature.

$$A_{l-g} \approx \frac{mg(H_{sat} - H_{in})}{\bar{q}} \qquad A_g \approx \frac{mg(H_{out} - H_{sat})}{\bar{q}} \qquad Al \approx 1 - Al - A_{l-g} \tag{15}$$

4. Conclusion

A method utilizing return fine particles instead of molten salt for the flexibility enhancement of thermal power plants has been proposed. Series-connectable experimental setup was constructed, and charging/discharging experiments of several tens of kilowatts were conducted. Results indicate that:

(1) Steam at 250 °C achieves the highest charging power of approximately 10 kW owing to its smaller particle-specific heat capacity and better charging capability against ambient temperature, followed by 400 °C, 350 °C, and 300 °C. Thermal buoyancy induced by 400 °C steam reduces the thermal resistance of the bed, thereby facilitating heat transfer. The highest average charging power and convective heat transfer coefficient at 250 °C are 7.42 kW and 314.37 W/(m^2·K), respectively. Next is 400 °C steam with values of approximately 5.67 kW and 222.91 W/(m^2·K). However, the lower specific heat capacity leads to the lowest charging efficiency at 250 °C. Considering multiple indicators, charging at 400 °C exhibits significant advantages;

(2) Bed layers at 350 °C and 400 °C can continuously produce superheated steam above 250 °C for 12 min, maintaining a power generation of 30 kW. Due to the extensive phase transition region and high steam generation rate, the bed layer at 350 °C exhibits the highest discharge efficiency, approximately 75 %. At 400 °C, the discharge efficiency is the second-highest due to larger heat exchange differences, approximately 66 %;

(3) Movement speed and area proportion of the phase transition region at different bed temperatures were determined, with speed of 10–30 mm/s. The phase transition region at 400 °C eventually occupied 75 % of the device volume, while the 350 °C bed layer only occupied 65 %. During the depletion stage, the superheating section occupied only 10–20 % of the area;

(4) Extracting steam above 350 °C for energy storage offers higher charging and discharging efficiency and is suitable for multiple charging cycles, making it the optimal choice.

CRediT authorship contribution statement

Xiang Liu: Writing – original draft, Visualization, Validation, Supervision, Software, Investigation, Formal analysis, Data curation. **Lijia Wei:** Writing – review & editing, Data curation. **Laiquan Lv:** Writing – review & editing, Conceptualization. **Hao Zhou:** Project administration, Funding acquisition, Conceptualization.

Declaration of competing interest

The authors declare that they have no known competing financial interests or personal relationships that could have appeared to influence the work reported in this paper.

Acknowledgments

Supported by "the Fundamental Research Funds for the Central Universities (2022ZFJH04)".

Data availability

Data will be made available on request.

References

[1] Organization GEIDaC, Carbon neutrality goal established wind power development will be on the fast track by 2021, Available from: https://www.geidco.org.cn/2021/0322/3765.shtml, 2024.
[2] Y. Zhao, M. Liu, C. Wang, X. Li, D. Chong, J. Yan, Increasing operational flexibility of supercritical coal-fired power plants by regulating thermal system configuration during transient processes, Appl. Energy 228 (2018) 2375–2386.
[3] Z.-k. Feng, W.-j. Niu, W.-c. Wang, J.-z. Zhou, C.-t. Cheng, A mixed integer linear programming model for unit commitment of thermal plants with peak shaving operation aspect in regional power grid lack of flexible hydropower energy, Energy 175 (2019) 618–629.
[4] Z. Wang, M. Liu, Y. Zhao, C. Wang, D. Chong, J. Yan, Flexibility and efficiency enhancement for double-reheat coal-fired power plants by control optimization considering boiler heat storage, Energy 201 (2020) 117594.
[5] Y.-L. Xin, T. Zhao, X. Chen, K.-L. He, H. Ma, Q. Chen, Heat current method-based real-time coordination of power and heat generation of multi-CHP units with flexibility retrofits, Energy 252 (2022) 124018.
[6] C. Brunner, G. Deac, S. Braun, C. Zöphel, The future need for flexibility and the impact of fluctuating renewable power generation, Renew. Energy 149 (2020) 1314–1324.
[7] J.D. Wojcik, J. Wang, Technical feasibility study of thermal energy storage integration into the conventional power plant cycle, Energies 10 (2017).
[8] D. Li, Y. Hu, W. He, J. Wang, Dynamic modelling and simulation of a combined-cycle power plant integration with thermal energy storage, in: 2017 23rd International Conference on Automation and Computing (ICAC), 2017, pp. 1–6.
[9] L. Miao, M. Liu, K. Zhang, J. Yan, Design and performance evaluation of thermal energy storage system with hybrid heat sources integrated within a coal-fired power plant, J. Energy Storage 82 (2024) 110611.
[10] L. Miao, M. Liu, K. Zhang, Y. Zhao, J. Yan, Energy, exergy, and economic analyses on coal-fired power plants integrated with the power-to-heat thermal energy storage system, Energy 284 (2023) 129236.
[11] H. Zhang, L. Sun, H. Zhao, X. Zhang, G. Xin, Thermodynamic analysis of the coal-fired combined heat and power units integrated with steam ejectors and thermal storage, J. Energy Storage 90 (2024) 111869.
[12] D. Li, J. Wang, Study of supercritical power plant integration with high temperature thermal energy storage for flexible operation, J. Energy Storage 20 (2018) 140–152.
[13] H. Tang, M. Liu, K. Zhang, S. Zhang, C. Wang, J. Yan, Performance evaluation and operation optimization of a combined heat and power plant integrated with molten salt heat storage system, Appl. Therm. Eng. 245 (2024) 122848.
[14] X. Liu, L. Zhang, K. Jin, X. Xue, H. Zhou, Integration model and performance analysis of coupled thermal energy storage and ejector flexibility retrofit for 600 MW thermal power units, J. Clean. Prod. 428 (2023) 139337.
[15] X. Liu, K. Jin, X. Xue, L. Zhang, H. Zhou, Performance and economic analysis of steam extraction for energy storage to molten salt with coupled ejector and thermal power units, J. Energy Storage 72 (2023) 108488.
[16] V.D. Stevanovic, M.M. Petrovic, S. Milivojevic, M. Ilic, Upgrade of the thermal power plant flexibility by the steam accumulator, Energy Convers. Manag. 223 (2020) 113271.
[17] M. Richter, G. Oeljeklaus, K. Görner, Improving the load flexibility of coal-fired power plants by the integration of a thermal energy storage, Appl. Energy 236 (2019) 607–621.
[18] H. Jouhara, N. Khordehgah, S. Almahmoud, B. Delpech, A. Chauhan, S.A. Tassou, Waste heat recovery technologies and applications, Therm. Sci. Eng. Prog. 6 (2018) 268–289.
[19] H.M. Ali, T.-u. Rehman, M. Arıcı, Z. Said, B. Duraković, H.I. Mohammed, et al., Advances in thermal energy storage: fundamentals and applications, Prog. Energy Combust. Sci. 100 (2024) 101109.
[20] M.M.S. Ahmed, M.J. Hasan, M.S. Chowdhury, M.K. Rahman, M.S. Islam, M. S. Hossain, et al., Prospects and challenges of energy storage materials: a comprehensive review, Chem. Eng. J. Adv. 20 (2024) 100657.
[21] (NEA) NEA, Notice of the Comprehensive Department of the National Energy Administration on the safety examination of molten salt heat storage and other comprehensive utilization of energy projects, Available from: https://zfxxgk.nea.gov.cn/2023-05/17/c_1310720738.htm, 2023.
[22] J. Han, Y. Yang, H. Hou, Advances in sensible heat storage technology for solar thermal power generation, Renew. Energy 32 (07) (2014) 901–905.
[23] B. Yang, X. Li, J. Zhao, Advances in mobile thermal storage technology, Chem. Ind. Eng. Prog. 32 (03) (2013) 515–520.
[24] G. Hailu, P. Hayes, M. Masteller, Long-term monitoring of sensible thermal storage in an extremely cold region, Energies 12 (2019).
[25] P.M. Cuce, Box type solar cookers with sensible thermal energy storage medium: a comparative experimental investigation and thermodynamic analysis, Sol. Energy 166 (2018) 432–440.
[26] H. Caliskan, I. Dincer, A. Hepbasli, Energy, exergy and sustainability analyses of hybrid renewable energy based hydrogen and electricity production and storage systems: modeling and case study, Appl. Therm. Eng. 61 (2) (2013) 784–798.
[27] M.M.S. Al-Azawii, C. Theade, M. Danczyk, E. Johnson, R. Anderson, Experimental study on the cyclic behavior of thermal energy storage in an air-alumina packed bed, J. Energy Storage 18 (2018) 239–249. ISSN 2352-152X, https://doi.org/10.1016/j.est.2018.05.008.
[28] E. Özrahat, S. Ünalan, Thermal performance of a concrete column as a sensible thermal energy storage medium and a heater, Renew. Energy 111 (2017) 561–579.
[29] G.S. Warkhade, A.V. Babu, S. Mane, K. Ganesh Babu, Experimental investigation of sensible thermal energy storage in small sized, different shaped concrete material packed bed, World J. Eng. 13 (5) (2016) 386–393.
[30] K. Vigneshwaran, G.S. Sodhi, P. Muthukumar, A. Guha, S. Senthilmurugan, Experimental and numerical investigations on high temperature cast steel based sensible heat storage system, Appl. Energy 251 (2019) 113322.
[31] C. Guan, H. Lu, L. Zhang, Z. Yu, Regulation of the output temperature in a novel water heating system using solid graphite as sensible heat thermal energy storage medium: effects of water tank, Energy Rep. 6 (2020) 160–171.
[32] L. Zhang, L. Qiao, E. Wang, C. Guan, L. Fan, Z. Yu, Thermal performance of a novel high-temperature sensible heat thermal storage steam generation system using solid graphite as material, J. Energy Storage 64 (2023) 107204.
[33] Z. Lai, Characterization of Sintering and Energy Storage in Granular Stacked Beds, Zhejiang University, 2022.
[34] M. Ji, L. Lv, S. Huang, A. Zhang, H. Zhou, Experimental study of thermal energy storage system for solid particles/ heat transfer oil in shell and tube heat exchangers with H-shaped fins, J. Clean. Prod. 434 (2024) 139943.
[35] L. Lv, S. Huang, H. Zhou, Heat transfer and thermal performance investigation on a visualized latent heat storage system in pilot-scale: scalable medium-temperature thermal energy storage system, J. Clean. Prod. 426 (2023) 139141.
[36] W.-T. Ji, D.-C. Zhang, Y.-L. He, W.-Q. Tao, Prediction of fully developed turbulent heat transfer of internal helically ribbed tubes – an extension of Gnielinski equation, Int. J. Heat Mass Transf. 55 (4) (2012) 1375–1384.
[37] X. Liu, F. Wu, L. Lv, L. Wei, H. Zhou, Performance of solid particles as thermal storage media in thermal power flexibility retrofits: effects of charging and discharging flow rates on single piece stacking bed, Energy 308 (2024) 132950.
[38] C. He, J. Lu, J. Ding, W. Wang, Y. Yuan, Heat transfer and thermal performance of two-stage molten salt steam generation system, Appl. Energy 204 (2017) 1231–1239.